JOURNAL OF SPACECRAFT AND ROCKETS
Vol. 42, No. 4, July–August 2005

Aerothermodynamic Performance Analysis of Hypersonic Flow on Power Law Leading Edges

Wilson F. N. Santos*
National Institute for Space Research, 12630-000 Cachoeira Paulista-SP, Brazil
and
Mark J. Lewis†
University of Maryland, College Park, Maryland 20742

A numerical study is reported on power-law-shaped leading edges situated in a rarefied hypersonic flow. The work is motivated by interest in investigating the flowfield properties of power-law-shaped leading edges as possible candidates for blunting geometries of hypersonic leading edges because power-law leading-edge shapes have both blunt (infinite body slope at the nose) and sharp (zero radius of curvature at the nose) characteristics. The sensitivity of the stagnation point heating, total drag, and shock wave standoff distance to shape variations of such leading edges is calculated by using the direct simulation Monte Carlo method. Comparisons based on equivalent stagnation point heating, equivalent total drag, and equivalent shock standoff distance are made between power law shapes and round leading edges. For the flow conditions considered, round leading edges provide lower drag and smaller shock standoff distance than power law leading edges for equivalent stagnation point heating. It was also found that power law shapes have smaller shock standoff distance and larger stagnation point heating than the round leading edges for equivalent total drag.

Nomenclature

A = constant in power law body equation
a = speed of sound, m/s
C_d = drag coefficient, $2F/\rho_\infty V_\infty^2 H$
C_f = skin friction coefficient, $2\tau_w/\rho_\infty V_\infty^2$
C_h = heat transfer coefficient, $2q_w/\rho_\infty V_\infty^3$
C_p = pressure coefficient, $2(p_w - p_\infty)/\rho_\infty V_\infty^2$
F = drag force, N
H = body height at the base, m
Kn = Knudsen number, λ/l
L = body length, m
l = characteristic length, m
M = Mach number, V/a
n = body power law exponent
p = pressure, N/m^2
q = heat flux, W/m^2
R_c = radius of curvature, m
Re = Reynolds number, $\rho V l/\mu$
R_N = round leading-edge nose radius, m
S = dimensionless arc length, s/λ_∞
s = arc length, m
T = temperature, K
V = velocity, m/s
$\bar{V}$ = volume, m^3
x, y = Cartesian axes in physical space, m
Δ = shock wave standoff distance, m
η = coordinate normal to body surface, m
θ = wedge half-angle, body slope angle, deg
λ = mean free path, m
ξ = coordinate tangent to body surface, m
ρ = density, kg/m^3
τ = shear stress, N/m^2

Subscripts

eqv = equivalent
pwr = power law
w = wall conditions
0 = stagnation point
∞ = freestream conditions

Introduction

WITH the renewed interest in aerodynamically efficient hypersonic vehicles, the waverider configuration has been considered as a promising concept for a high-performance hypersonic design. The waverider, originally proposed by Nonweiler,[1] is a shape designed analytically with infinitely sharp leading edge for shock wave attachment. The shock wave acts as a barrier to prevent spillage of higher pressure airflow from the lower side of the vehicle to the upper side, resulting in a significantly high lift-to-drag ratio, compared to other conventional hypersonic vehicles.

Nevertheless, for flight at hypersonic speeds, the vehicle leading edge should be sufficiently blunt to reduce the heat transfer rate to acceptable levels and, possibly, to allow for internal heat conduction. The use of blunt-nosed shapes tends to alleviate the aerodynamic heating problem because the heat flux for blunt bodies scales inversely with the square root of the nose radius. As a result, any practical waverider will have some degree of leading-edge bluntness for heat transfer, manufacturing or handling concerns. Moreover, leading-edge bluntness will displace the shock wave, and, hence, the aerodynamic performance[2] of the vehicle may be degraded from ideal conditions.

Power-law-shaped leading edges ($y \propto x^n$, $0 < n < 1$) may provide the required bluntness for heat transfer, manufacturing or handling concerns. This concept is based on the work of Mason and Lee,[3] who have pointed out that, for certain exponents, power law shapes exhibit aerodynamic properties similar to geometrically sharp shapes. They suggested the possibility of a difference between shapes that are geometrically sharp and shapes that behave aerodynamically as if they were sharp. Mason and Lee[3] showed that there is a class of body shapes given by $\frac{1}{2} < n < \frac{2}{3}$, for which the leading edge may behave aerodynamically like a blunt body, even though the leading-edge radius of curvature is zero. In addition, there is another class of body given by $\frac{2}{3} < n < 1$ for which the leading edge may behave like aerodynamically sharp body because the derivative of the

---

Received 25 March 2004; revision received 15 June 2004; accepted for publication 5 July 2004.

*Researcher, Combustion and Propulsion Laboratory. Member AIAA.

†Professor, Aerospace Engineering Department. Associate Fellow AIAA.

pressure coefficient with respect to the body coordinates $\mathrm{d}C_p/\mathrm{d}s$ approaches $-\infty$ at $x = 0$, even though the leading-edge bluntness is infinite. Their analysis describes the details of the geometry and aerodynamics of low-drag axisymmetric bodies by using Newtonian theory. However, one of the important aspects of the problem, stagnation point heat transfer, was not considered.

A great deal of work[4–13] has been carried out recently on the power law form representing blunt geometries. The major interest has been considering the power law shape as possible candidates for blunting geometries of hypersonic leading edges, such as hypersonic waverider vehicles that lately have been considered for high-altitude/low-density applications.[14–17]

Santos and Lewis[4] have investigated the sensitivity of the pressure gradient and the stagnation point heating to shape variations of such leading edges for the idealized situation of two-dimensional rarefied hypersonic flow at zero angle of incidence. Through the use of the direct simulation Monte Carlo (DSMC) method, they showed that the pressure gradient on the power law shapes in a rarefied environment is in agreement with that obtained by Mason and Lee[3] by employing Newtonian analysis. Santos and Lewis[4] also found that the stagnation point heating behavior for power law leading edges with finite radius of curvature ($n = \frac{1}{2}$) followed that predicted for classical blunt body, that is, the heating rate on blunt bodies is inversely proportional to the square root of curvature radius at the stagnation point. For those power law leading edges with zero radii of curvature ($n > \frac{1}{2}$), the stagnation point heating is not a function of the curvature radius in the vicinity of the leading edges, but agrees with the classical blunt-body behavior predicted by the continuum flow far from the stagnation point.

The knowledge of the flowfield structure and the aerodynamic surface quantities at zero angle of attack is not sufficient to predict with certainty the flow characteristics over these shapes with incidence. In this context, Santos and Lewis[5] have investigated the essential characteristics of the angle-of-attack effect on both pressure gradient and stagnation point heating for power law bodies defined by exponents of $\frac{1}{2}$, $\frac{2}{3}$, and $\frac{3}{4}$ and positive angle of attack with 5, 8, and 12 deg of incidence. It was found that, even though at incidence, the pressure gradient $\mathrm{d}C_p/\mathrm{d}s \to -\infty$ as $x \to 0$ along the both windward and leeward sides of the power law leading edge for the $n = \frac{3}{4}$ case. Thus, the leading edge with $n = \frac{3}{4}$ produces a flowfield that does not exhibit classical blunt-body behavior and can be considered as if it were sharp for the calculation of pressure distribution. It was also found that the heat flux to power-law-shaped leading edges followed that for classical blunt body far from the nose of the leading edges in that it is inversely proportional to the square root of the curvature radius. This dependence with the radius of curvature was more significant in the leeward side than that in the windward side with increasing the angle of attack, and it disappeared in the vicinity of the stagnation point.

Finally, O'Brien and Lewis[6] have examined power-law-shaped leading edges for possible use on hypersonic waverider vehicles. A numerical analysis was performed considering a two-dimensional inviscid flow by solving the Euler equations. Results were compared to a corresponding circular cylinder to determine which geometry would be better suited as a blunting profile. Their analysis showed that circular cylinders provide smaller shock standoff and drag for equivalent stagnation point heating under the range of conditions investigated.

The emphasis of this work is to compare power law leading edges with round leading edges to determine which geometry is better suited as a blunting profile in terms of stagnation point heating, total drag coefficient, and shock wave standoff distance. Two methods of comparison will be investigated: 1) Power law leading edges are compared to a corresponding round leading edge, which generates the power law shapes. 2) Power law leading edges are compared to an equivalent round leading edge, which is generated from the computational results for the power law shapes. The equivalent round leading edge will yield the same stagnation point heating, the same drag coefficient, or the same shock wave standoff distance as the computed solutions presented for power law shapes. Thus, for the equivalent stagnation point heating, for instance, the total drag coefficient and the shock standoff distance will be the basis of comparison between these leading edges and they will determine which geometry performs better.

The focus of the present study is the low-density region in the upper atmosphere, where numerical gas-kinetic procedures are available to simulate hypersonic flows. High-speed flows under low-density conditions deviate from a perfect-gas behavior because of the excitation of rotation, vibration, and dissociation. At high altitudes, and, therefore, low density, the molecular collision rate is low and the energy exchange occurs under nonequilibrium conditions. In such a circumstance, the degree of molecular nonequilibrium is such that the Navier–Stokes equations are inappropriate. Alternatively, the DSMC method is used to calculate the rarefied hypersonic two-dimensional flow on the leading-edge-shapes.

Leading-Edge Geometry Definition

In dimensional form, the body power law shapes are given by the following expression:

$$y = Ax^n \tag{1}$$

where n is the power law exponent and A is the power law constant that is a function of n.

The power law shapes are modeled by assuming a sharp leading edge of half angle θ with a circular cylinder of radius R inscribed tangent to this wedge. The power law shapes, inscribed between the wedge and the cylinder, are also tangent to them at the same common point where they have the same slope angle. A leading-edge half-angle of 10 deg, a circular cylinder diameter of 10^{-2} m, and power law exponents of $\frac{1}{2}$, 0.6, $\frac{2}{3}$, 0.7, $\frac{3}{4}$, and 0.8 were assumed.

From geometric considerations, the power law constant A is obtained by matching slopes for the wedge, circular cylinder, and power law body at the tangency point. The common body height H at the tangency point is equal to $2R\cos\theta$, and the body length L from the nose to the tangency point in the axis of symmetry is given by $nH/2\tan\theta$.

The round leading edges are modeled by following the same procedure adopted for the power law leading edges. Figure 1 shows this construction for power law leading edge of $n = \frac{1}{2}$ and a round leading edge with nose radius $R_N/\lambda_\infty = 0.962$, where λ_∞ is the molecular freestream mean free path.

It was assumed that the leading edges are infinitely long, but only the length L is considered because the wake region behind the leading edges is not of interest in this investigation.

Computational Method and Procedure

It is well known that neither the continuum flow equations nor the collisionless flow equations are valid to predict leading-edge aerothermodynamic characteristics throughout the transitional flow regime. At this time, it appears that the DSMC method[18] is the most accurate and credible procedure for computing leading-edge flowfield and surface effects in the transitional flow regime.

The DSMC method simulates real-gas flows with various physical processes by means of a huge number of modeling particles, each of which is a typical representative of great number of real-gas molecules. DSMC models the flow as being a collection of discrete particles, each one with a position, velocity, and internal energy. The position, velocity, and internal energy of these particles are stored

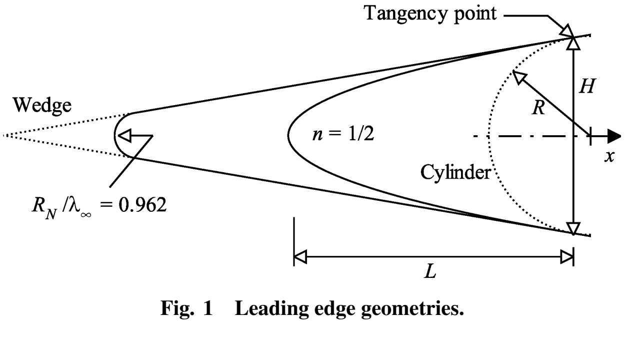

Fig. 1 Leading edge geometries.

by the computer and are modified with time as the particles move and undergo representative collisions and boundary interactions in simulated physical space.

The molecular collisions are modeled using the variable hard sphere (VHS) molecular model.[19] This model employs the simple hard sphere angular scattering law so that all directions are equally possible for postcollision velocity in the center-of-mass frame of reference. Nevertheless, the collision cross section depends on the relative speed of colliding molecules.

The energy exchange between kinetic and internal modes is controlled by the Borgnakke–Larsen statistical model.[20] The essential feature of this model is that a fraction of the collisions is treated as completely inelastic, and the remainder of the molecular collisions is regarded as elastic. Simulations are performed using a nonreacting gas model consisting of two chemical species, N_2 and O_2. Energy exchanges between the translational and internal modes are considered. For this study, the relaxation numbers of 5 and 50 were used for the rotation and vibration, respectively. The effective number of degrees of freedom in the partially excited vibrational states is calculated from the harmonic oscillator theory.

The flowfield is divided into a number of regions, which are subdivided into computational cells. The cells are further subdivided into four subcells, two subcells/cell in each direction. The cell provides a convenient reference for the sampling of the macroscopic gas properties, whereas the collision partners are selected from the same subcell for the establishment of the collision rate. The dimensions of the cells must be such that the change in flow properties across each cell is small. The linear dimensions of the cells should be small in comparison with the scale length of the macroscopic flow gradients normal to the streamwise directions, which means that the cell dimensions should be of the order of the local mean free path or even smaller.[18] Time is advanced in discrete steps such that each step is small in comparison with the mean collision time.[18]

The computational domain used for the calculations is made large enough so that the upstream and side boundaries can be specified as freestream conditions. A schematic view of the computational domain is given in Fig. 2. The advantage of flow symmetry is taken into account to reduce the computational domain. Diffuse reflection with complete thermal accommodation is the condition applied to the body surface. In this model, the reflection of the impinging molecules is not related to the preimpingement state of the molecules; the outgoing velocity of the molecules is randomly assigned according to a half-range Maxwellian distribution determined by the wall temperature. At the boundary on the symmetry plane, all flow gradients normal to the plane are zero. At the molecular level, this plane is equivalent to a specular reflecting boundary. The outer computational boundary is the freestream side, through which simulated molecules can enter and exit. The flow at the downstream outflow boundary is predominantly supersonic, and vacuum conditions are specified.[18]

The numerical accuracy of the DSMC method depends on the grid resolution chosen, as well as the number of particles per computational cell. Both effects were investigated to determine the number of cells and the number of particles required to achieve grid independent solutions for the thermal nonequilibrium flow that arises near the nose of the leading edges. A discussion of both effects on the aerodynamic surface quantities is given by Santos and Lewis[9] for round leading edges and by Santos and Lewis[10] for power law leading edges.

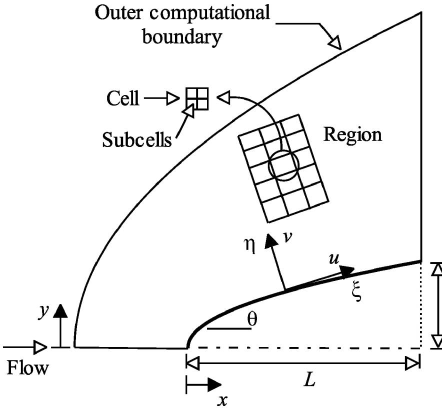

Fig. 2 Schematic of computational domain.

Table 1 Freestream and flow conditions

Parameter	Value	Unit
Temperature T_∞	220.0	K
Pressure p_∞	5.582	N/m^2
Density ρ_∞	8.753×10^{-5}	kg/m^3
Viscosity μ_∞	1.455×10^{-5}	N · s/m^2
Number density n_∞	1.8209×10^{21}	m^{-3}
Mean free path λ_∞	9.03×10^{-4}	m
Molecular weight	28.96	kg/kg · mol
Molecular mass O_2	5.312×10^{-26}	kg
Molecular mass N_2	4.650×10^{-26}	kg
Molecular diameter O_2	4.01×10^{-10}	m
Molecular diameter N_2	4.11×10^{-10}	m
Mole fraction O_2	0.237	
Mole fraction N_2	0.763	
Viscosity index O_2	0.77	
Viscosity index N_2	0.74	

The conditions used for the numerical simulation of flow past the leading edges are those given by Santos and Lewis[4] and are summarized in Table 1.

The freestream velocity V_∞ is assumed to be constant at 3.56 km/s, which corresponds to a freestream Mach number M_∞ of 12. The wall temperature T_w is assumed constant at 880 K, chosen to be four times the freestream temperature. The overall Knudsen number is defined as the ratio of the molecular mean free path in the freestream gas to a characteristic dimension of the flowfield. In the present study, the characteristic dimension was defined as being the radius of the reference circular cylinder. Therefore, the freestream Knudsen number Kn_∞ corresponds to 0.0903. Finally, the freestream Reynolds number per meter Re_∞ is 2.1455×10^4.

Computational Results and Discussion

The purpose of this section is to discuss and to compare differences in the heat transfer, total drag, and shock wave standoff distance resulting from the DSMC simulations due to changes in the leading-edge shape.

Power Law Leading Edge

The heat flux q_w to the body surface is calculated by the net energy flux of the molecules impinging on the surface. The net heat flux is related to the sum of the translational, rotational, and vibrational energies of both incident and reflected molecules. A flux is regarded as positive if it is directed toward the surface. The heat flux is normalized by the freestream kinetic energy flux $\rho_\infty V_\infty^3/2$ and presented in terms of heat transfer coefficient C_h.

The heat transfer coefficient C_h is shown in Fig. 3 as a function of the dimensionless arc length S ($\equiv s/\lambda_\infty$) along the surface measured from the stagnation point. For comparison purpose, Fig. 3 also shows the heat transfer coefficient for the reference round leading edge (reference circular cylinder). It is seen that the heat transfer coefficient is sensitive to the power law exponent n near the stagnation point. It presents the maximum value in the stagnation point and drops off sharply a short distance away from the leading edge as the power law exponent increases. The leading-edge geometry effect can also be seen by comparing the computational results with that calculated by assuming free molecular flow.[18] Figure 4 presents this comparison for the heat transfer coefficient as a function of the body slope angle θ. These curves indicate that the heat transfer coefficient approaches the free molecular limit as the power law exponent increases.

The heat transfer coefficient at the stagnation point C_{h0} for the power law leading edges is presented in Table 2. These values were obtained by a curve-fitting process performed over the curves

Table 2 Heat transfer coefficient at stagnation point C_{h0} for power law leading edges

n	C_{h0}
1/2	0.605
0.6	0.730
2/3	0.785
0.7	0.821
3/4	0.858
0.8	0.879

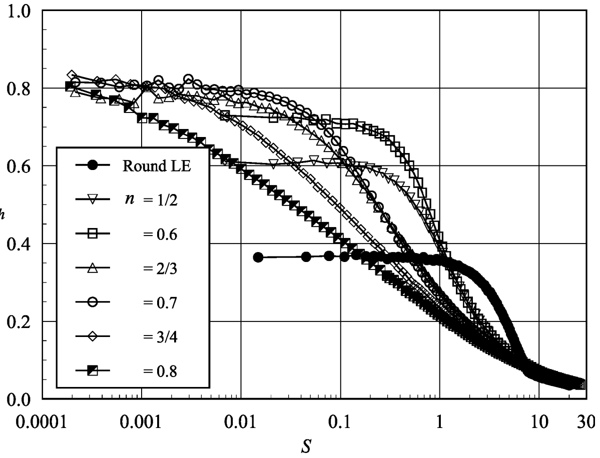

Fig. 3 Heat transfer coefficient C_h along the body surface for various power law bodies.

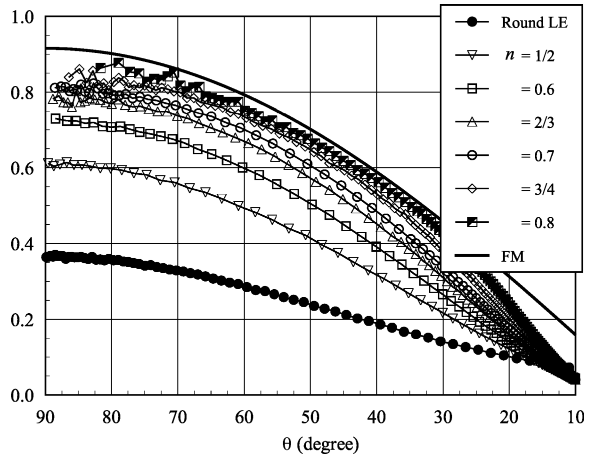

Fig. 4 Heat transfer coefficient C_h along the body surface as a function of body slope angle θ.

displayed in Fig. 4. For comparison purpose, the heat transfer coefficient at the stagnation point for the reference round leading edge is $C_{h0} = 0.366$. Therefore, C_{h0} for power law shapes with $n = \frac{1}{2}$ and 0.8 are 1.65 and 2.4 times, respectively, larger than that for the round leading-edge case.

Note that the first cell size along the body surface is crucial in the prediction of the stagnation point heating. As a reference, for the $n = 0.8$ case, a cell size, in terms of arc length, that corresponds a decrease of 4 deg in the body slope angle θ (an arc length defined by the distance from the stagnation point to the point on the body surface corresponding to a body slope angle of 86 deg) is the order of $s/\lambda_\infty \approx 10^{-7}$. The freestream mean free path λ_∞ is 9.03×10^{-4} m; then the arc length s is around 10^{-10} m for $\Delta\theta = 4$ deg, that is, the order of the molecule diameter, 4×10^{-10} m. For the $n = 0.8$ case investigated in this simulation, the first cell size on the body surface is about $s/\lambda_\infty \approx 5 \times 10^{-6}$. As a result, the size of the first cell is 10 times larger than the molecular diameter, and the body slope angle corresponding to the middle of the first cell is around 81 deg, as shown in Fig. 4. Therefore, the $n = 0.8$ case represents a thin body with a blunt nose ($dy/dx \to \infty$ at $x = 0$) and a body curvature in the neighborhood of the nose that changes dramatically at a considerable rate.

The drag on a surface in a gas flow results from the interchange of momentum between the surface and the molecules colliding with the surface. The total drag is obtained by the integration of the pressure p_w and shear stress τ_w distributions along the body surface. In an effort to understand the effects of the pressure and the shear stress acting on the surface of the leading edges, both forces will be described in this section.

The pressure p_w on the body surface is calculated by the sum of the normal momentum fluxes of both incident and reflected molecules at each time step. Results are presented in terms of pressure coefficient C_p and the dimensionless distance S along the body surface.

The effects of the power law exponent on the pressure coefficient are shown in Fig. 5 for power law exponents of $\frac{1}{2}$, 0.6, $\frac{2}{3}$, 0.7, $\frac{3}{4}$, and 0.8. Figure 5 also shows the pressure coefficient for the round leading edge used as a reference. It is seen that the pressure coefficient follows the same trend as that presented by the heat transfer coefficient. It presents the maximum value at the stagnation point and decreases fast along the body surface as the power law exponent increases.

The variation of the pressure coefficient shown in Fig. 5 is examined from another viewpoint in Fig. 6. Hence, the pressure coefficient is presented as a function of the body slope angle θ. Plotted along with the computational solutions for power law shapes is the pressure coefficient predicted by the free molecular flow

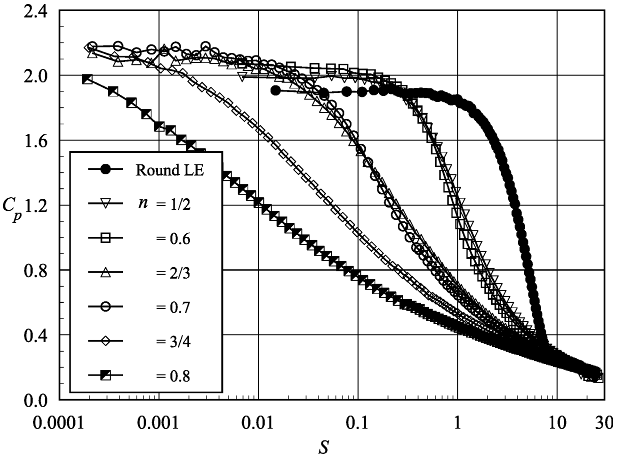

Fig. 5 Pressure coefficient C_p along the body surface for various power law bodies.

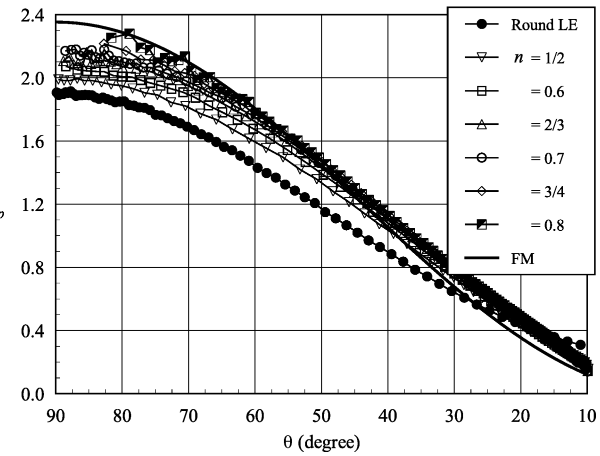

Fig. 6 Pressure coefficient C_p along the body surface as a function of body slope angle θ.

equations.[18] It is also apparent from Fig. 6 that the pressure coefficient approaches the value predicted by the free molecular flow in the vicinity of stagnation region as the power law shapes become aerodynamically sharp[4] ($n \to 0.8$).

The shear stress τ_w on the body surface is calculated by averaging the tangential momentum transfer of the molecules impinging on the surface. For the diffuse reflection model imposed for the gas–surface interaction, reflected molecules have a tangential moment equal to zero because the molecules essentially lose, on average, their tangential velocity component. Results are normalized by freestream dynamic pressure $\rho_\infty V_\infty^2/2$ and presented in terms of the skin-friction coefficient C_f and the dimensionless arc length S along the surface measured from the stagnation point.

The leading-edge geometry effect on the skin-friction coefficient C_f is shown in Fig. 7 for power law exponents of $\frac{1}{2}$, 0.6, $\frac{2}{3}$, 0.7, $\frac{3}{4}$, and 0.8. Along the surface, the value of C_f starts from zero at the stagnation point, increases to a maximum value near the leading edge, and decreases downstream along the body surface. Larger n leads to higher peak value for the skin-friction coefficient. Also, larger n displaces the peak value to near the stagnation point. The skin-friction coefficient presents interesting features as it is plotted as a function of the body slope angle θ. Figure 8 shows these features, as well as a comparison with the skin-friction coefficient, by assuming a free molecular flow situation. As can be seen, the free molecular flow exhibits the maximum value for the skin-friction coefficient at 45-deg station. Similarly, the maximum values for the power law leading edges occur very close to the same station, that is, 45 deg.

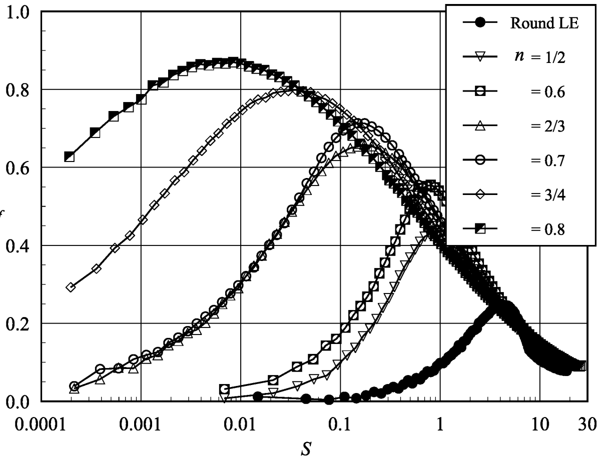

Fig. 7 Skin-friction coefficient C_f along the body surface for various power law bodies.

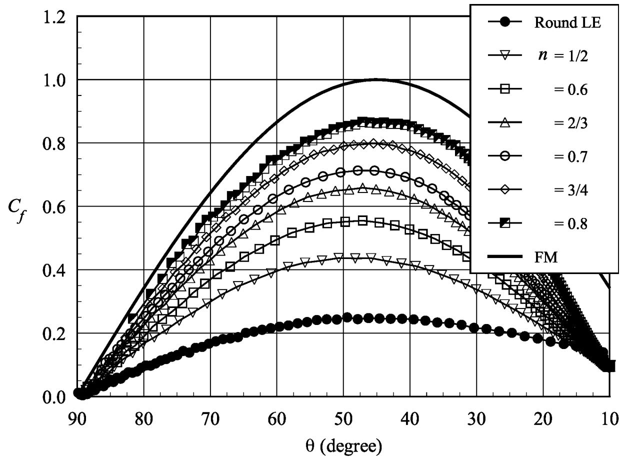

Fig. 8 Skin-friction coefficient along the body surface as a function of body slope angle θ.

Table 3 Dimensionless shock wave standoff distance Δ/λ_∞ for power law leading edges

n	Δ/λ_∞
1/2	0.665
0.6	0.457
2/3	0.330
0.7	0.289
3/4	0.216
0.8	0.166

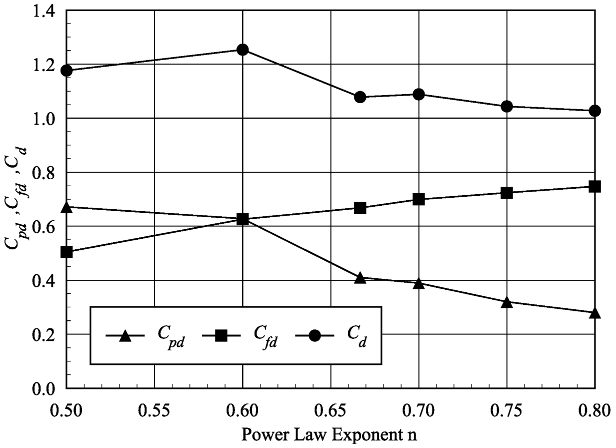

Fig. 9 Pressure drag C_{pd}, skin-friction drag C_{fd}, and total drag C_d coefficients as a function of body power law exponent n.

The total drag is obtained by the integration of the pressure p_w and shear stress τ_w distributions from the nose of the leading edge to the station L (Fig. 1), which corresponds to the tangent point common to all of the body shapes. Note that the values for the total drag presented in this section were obtained by assuming the shapes acting as leading edges. Consequently, no base pressure effects were taken into account on the calculations. The DSMC results for total drag are normalized by $\rho_\infty V_\infty^2 H/2$ and presented as total drag coefficient C_d and its components of pressure drag C_{pd} and skin-friction drag C_{fd} coefficients.

The extent of the changes in the total drag coefficient C_d with increasing the power law exponent is demonstrated in Fig. 9. As $n \to \frac{1}{2}$, the pressure drag contribution to the total drag coefficient is larger than that presented by the skin-friction drag, a characteristic of a blunt body. However, as $n \to 0.8$, the total drag coefficient is dominated by the skin-friction drag, a characteristic of a sharp body. The drag coefficient for the $n = \frac{1}{2}$ case is around 17% higher than that for the $n = 0.8$ case. For the reference round leading-edge case, the pressure drag C_{pd}, skin-friction drag C_{fd}, and total drag C_d coefficients are 1.352, 0.167, and 1.519, respectively. Thus, compared to the power law shapes, the reference round leading edge presents high value to the total drag coefficient, where the major contribution is given by the pressure drag coefficient. As a reference, the total drag for the reference round leading edge is 15 and 31.5% larger than those for power law leading edges with n equal to $\frac{1}{2}$ and 0.8, respectively.

The shock wave standoff distance, defined as the distance from the shock wave center to the nose of the leading edge along the stagnation streamline, has been already calculated by Santos and Lewis in Ref. 10, in which the procedure used to obtain the shock wave standoff distance is described in detail. Therefore, only the results will be presented in this work.

Table 3 lists the shock wave standoff distance Δ, normalized by λ_∞, for the power law leading edges investigated. According to Table 3, there is a discrete shock standoff distance for all cases investigated. Moreover, the shock standoff distance decreases with increasing power law exponent n, that is, as the leading edge becomes aerodynamically sharp. Compared to power law shapes, the reference round leading edge provides a larger shock detachment, that is, $\Delta/\lambda_\infty = 1.645$. This value is about 2.5 times larger than the $n = \frac{1}{2}$ case and is one order of magnitude larger then the $n = 0.8$ case.

The displacement of the shock wave is especially undesirable in a waverider geometry because this hypersonic configuration usually depends on shock wave attachment at the leading edge to achieve its high lift-to-drag ratio at high-lift coefficient. Shock wave detachment will allow pressure leakage from the lower surface of the vehicle to the upper surface, thereby degrading the aerodynamic performance of the vehicle. In this context, the power law leading edges seem to be more appropriate than the reference round leading edge because they present reduced shock wave detachment distances as compared to round leading edge. Nevertheless, smaller shock detachment distance is associated with a higher heat load to the nose of the leading edge.

Round Leading Edge

To compare power law leading edge with round leading edge, it becomes necessary to determine the dependence of heat transfer, total drag, and shock standoff distance for round leading edge on the nose radius. Thus, DSMC simulations were performed for four round leading edges, besides the reference round leading edge (circular cylinder), with nose radii R_N/λ_∞ of 0.02, 0.1, 1.0, and 2.0, which correspond to overall Knudsen number Kn_D of 25, 5, 0.5, and 0.25, respectively, by assuming the nose diameter as the characteristic length.

Distributions of the heat transfer coefficient C_h along the round leading-edge surface are shown in Fig. 10 with the dimensionless nose radius R_N/λ_∞ as a parameter. It is observed in Fig. 10 that altering the nose radius produces a substantial change in the heat transfer coefficient in the cylindrically blunt portion of the leading edge, provided that the gas–surface interaction is diffuse. The heat transfer coefficient presents the maximum value in the stagnation point and drops off sharply along the cylindrically blunt portion up to the cylinder/wedge junction. Also, the heat transfer coefficient in the stagnation region decreases with increasing the nose radius. This behavior seems to be in agreement with the continuum predictions for blunt body in that the heat flux scales inversely with the square root of the nose radius.

The nose radius effect can also be seen in a different way by comparing the DSMC computational results with those calculated by assuming free molecular flow. Figure 11 presents this comparison for the heat transfer coefficient as a function of the body slope angle θ. Similarly to power law shapes, these curves indicate that the heat transfer coefficient also approaches the free molecular limit ($C_{h0} = 0.915$) in the cylindrical portion of the round leading edge with reducing the nose radius. As expected, by the reducing of the nose radius, the leading edge becomes sharper and approaches the wedge leading edge shown in Fig. 1.

The heat transfer coefficient at the stagnation point C_{h0} is given in Table 4 for the nose radii investigated. These values were obtained by a curve fitting process performed over the curves shown in Fig. 11.

Table 4 Heat transfer coefficient at stagnation point C_{h0} for round leading edges

R_N/λ_∞	C_{h0}
0.02	0.883
0.1	0.824
1.0	0.630
2.0	0.532
5.5	0.366

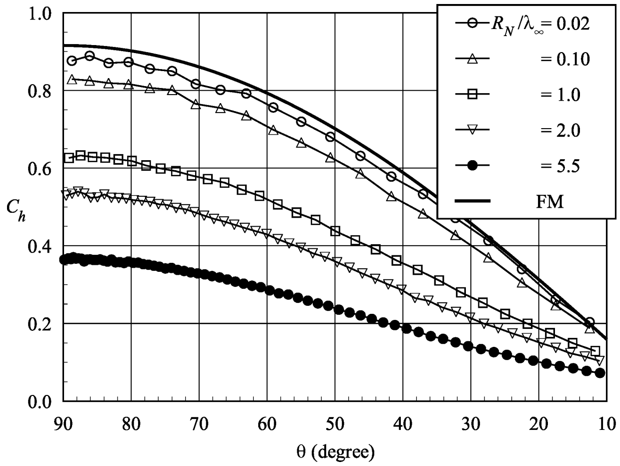

Fig. 11 Heat transfer coefficient C_h along the cylindrically blunt portion of the round leading edge as a function of body slope angle θ.

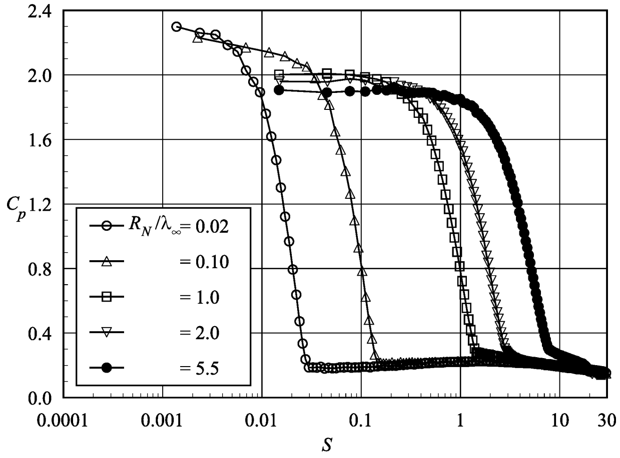

Fig. 12 Pressure coefficient C_p along the round leading edge surface for various nose radii.

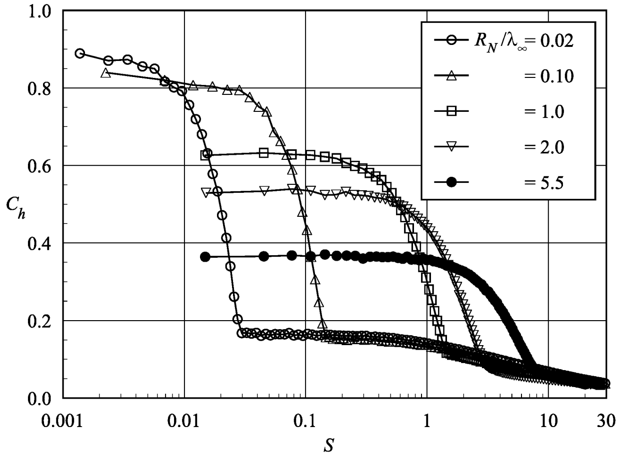

Fig. 10 Heat transfer coefficient C_h along the round leading-edge surface for various nose radii.

Distributions of the pressure coefficient C_p along the body surface for different nose radii are given in Fig. 12. According to Fig. 12, it is seen that the pressure coefficient follows the same trend as that presented by the heat transfer coefficient. The pressure coefficient presents the maximum value at the stagnation point and decreases rapidly in the cylindrically blunt portion of the leading edge. It is also verified that the pressure coefficient in the cylindrically blunt portion is one order of magnitude higher than the pressure coefficient in the wedge portion of the leading edge.

The pressure coefficient C_p acting on the cylindrical blunt portion of the leading edges is compared to that predicted by free molecular flow in Fig. 13, with the nose radius as a parameter. Note in Fig. 13 that the pressure coefficient also approaches that one predicted by free molecular flow ($C_{po} = 2.35$) for the smallest nose radius investigated, which corresponds to an overall Knudsen number Kn_D of 25.

Variations of the skin-friction coefficient C_f caused by changes in the nose radius of the leading edge are shown in Fig. 14 as a function of the dimensionless arc length S. As can be seen, the skin-friction coefficient increases from zero at the stagnation point to a

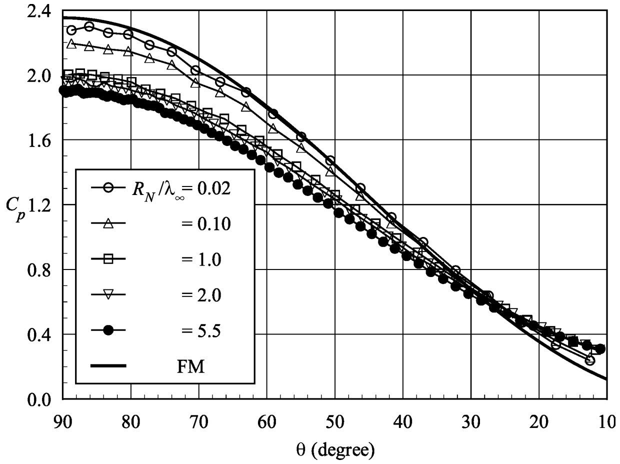

Fig. 13 Pressure coefficient C_p along the cylindrically blunt portion of the round leading edge as a function of body slope angle θ.

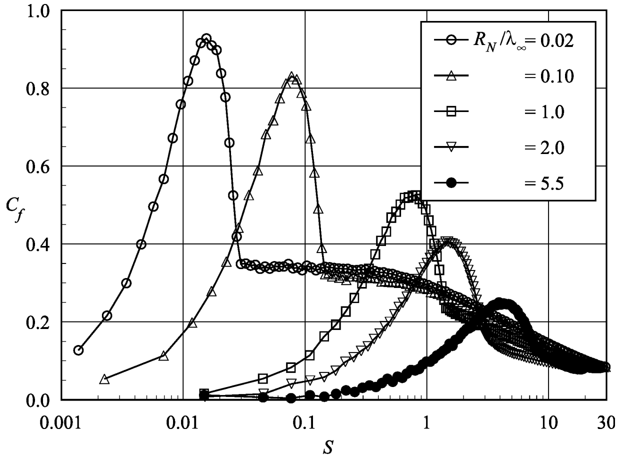

Fig. 14 Skin-friction coefficient C_f along the round leading-edge surface for various nose radii.

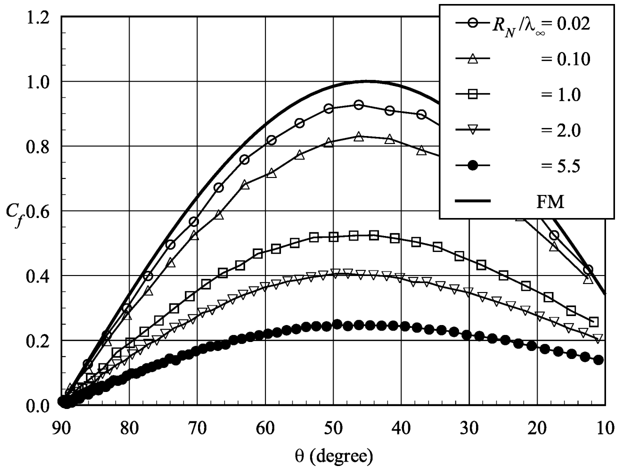

Fig. 15 Skin-friction coefficient C_f along the cylindrically blunt portion of the round leading edge as a function of body slope angle θ.

maximum that is located in the cylindrically blunt portion of the leading edge and decreases downstream along the body surface.

The skin-friction coefficient C_f from computational solution can be also compared to that predicted by considering free molecular flow. Figure 15 shows the comparison for the cylindrically portion of the leading edges as a function of the body slope angle θ. As can be seen, the round leading edges also exhibit the maximum value for the skin-friction coefficient around the 45-deg station.

Table 5 Dimensionless shock wave standoff distance Δ/λ_∞ for round leading edges

R_N/λ_∞	Δ/λ_∞
0.02	0.114
0.1	0.226
1.0	0.598
2.0	0.845
5.5	1.646

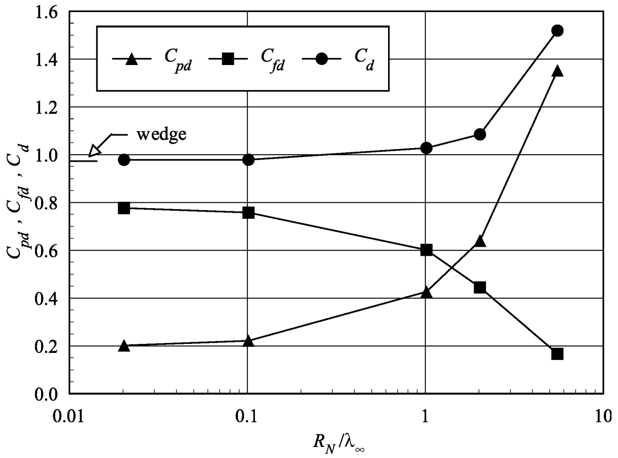

Fig. 16 Total drag coefficient for round leading edges as a function of nose radius.

The dependence of the total drag coefficient C_d on the nose radius is shown in Fig. 16. In Fig. 16, the contributions of the pressure drag C_{pd} and the skin-friction drag C_{fd} coefficients are also shown. As would be expected, the total drag for round leading edges approaches the wedge drag with decreasing the nose radius.

The dimensionless shock wave standoff distance Δ/λ_∞ for round leading edges is shown in Table 5. Similarly to power law leading edges, there is a discrete shock standoff distance for the round leading-edge cases investigated. In addition, the shock standoff distance decreases with diminishing nose radius. This is an expected result because shock standoff distance on a cylinder scales with the curvature radius.

Equivalent Nose Radius

The stagnation point heating, total drag, and shock wave standoff distance for power law leading edges have been compared to those for the reference round leading edge in the preceding sections. A second means of comparison between power law shapes and round leading edges is defined as equivalent round leading edge. Equivalent round leading edges, or equivalent nose radii, are found that have the same value of stagnation point heating, total drag, or shock standoff distance provided by the power law leading edges. For instance, by holding the stagnation point heating the same, the total drag and the shock standoff distance on the equivalent round leading edge may be compared to those for power law leading edges to determine which shape is better suited for leading-edge blunting. Afterward, a similar procedure is repeated for the total drag and for the shock standoff distance.

A summary of the computed data for the heat transfer coefficient at the stagnation point C_{h0}, the total drag coefficient C_d, and the shock standoff distance Δ/λ_∞ is shown in Figs. 17 and 18 for power law and round leading edges, respectively.

The stagnation point heating C_{h0} for each one of the power law shapes shown in Fig. 17 is used as an input in Fig. 18 to determine the equivalent nose radius $R_{N,\mathrm{eqv}}$. With the equivalent nose radius, the total drag and the shock standoff distance that correspond to the equivalent nose radius are also obtained from Fig. 18 itself.

The comparison of the total drag coefficient and the shock standoff distance for power law shapes and for round leading edges with equivalent nose radii that match power law body stagnation point

Table 6 Nose radius necessary for comparable stagnation point heating to power law shapes

n	$R_{N,\mathrm{eqv}}/\lambda_\infty$	$R/R_{N,\mathrm{eqv}}$	$C_{d,\mathrm{eqv}}/C_{d,\mathrm{pwr}}$	$\Delta_{\mathrm{eqv}}/\Delta_{\mathrm{pwr}}$	$\bar{V}_{\mathrm{eqv}}/\bar{V}_{\mathrm{pwr}}$
1/2	1.268	4.37	0.886	0.992	1.314
0.6	0.544	10.19	0.800	0.887	1.221
2/3	0.288	19.25	0.917	0.912	1.156
0.7	0.116	47.92	0.900	0.801	1.127
3/4	0.055	99.94	0.938	0.753	1.087
0.8	0.027	207.42	0.952	0.742	1.050

Table 7 Nose radius necessary for comparable total drag to power law shapes

n	$R_{N,\mathrm{eqv}}/\lambda_\infty$	$R/R_{N,\mathrm{eqv}}$	$C_{h0,\mathrm{eqv}}/C_{h0,\mathrm{pwr}}$	$\Delta_{\mathrm{eqv}}/\Delta_{\mathrm{pwr}}$	$\bar{V}_{\mathrm{eqv}}/\bar{V}_{\mathrm{pwr}}$
1/2	2.771	1.999	0.821	1.526	1.104
0.6	3.395	1.631	0.640	2.529	0.871
2/3	1.914	2.893	0.692	2.471	1.051
0.7	2.060	2.688	0.646	2.950	1.006
3/4	1.299	4.264	0.702	3.091	1.040
0.8	1.011	5.476	0.718	3.599	1.023

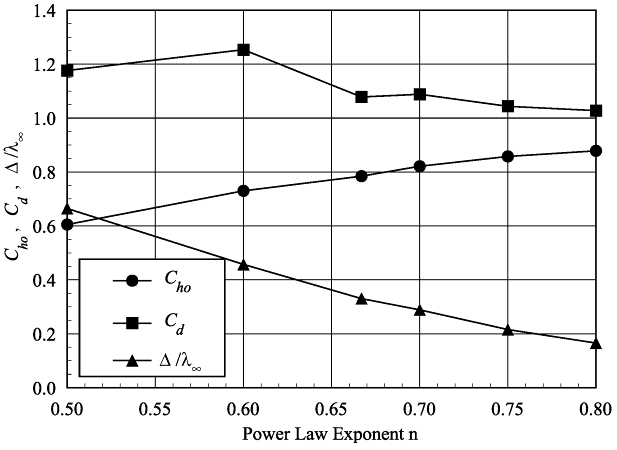

Fig. 17 Heat transfer coefficient at stagnation point C_{h0}, total drag C_d, and shock standoff distance Δ/λ_∞ for power law leading edges.

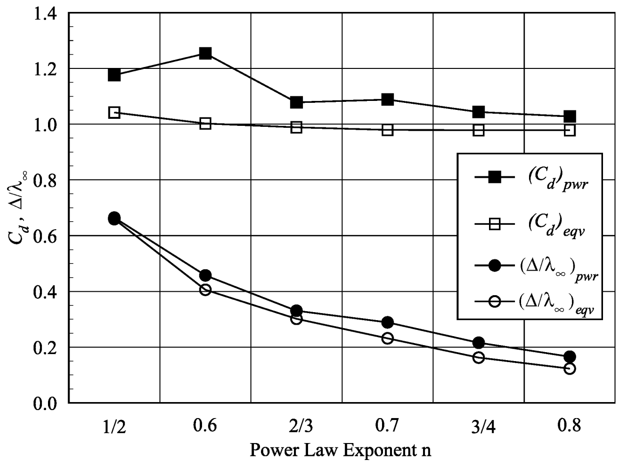

Fig. 19 Comparison of total drag coefficient and shock standoff distance for power law shapes and for equivalent round leading edges that match power law body stagnation point heating.

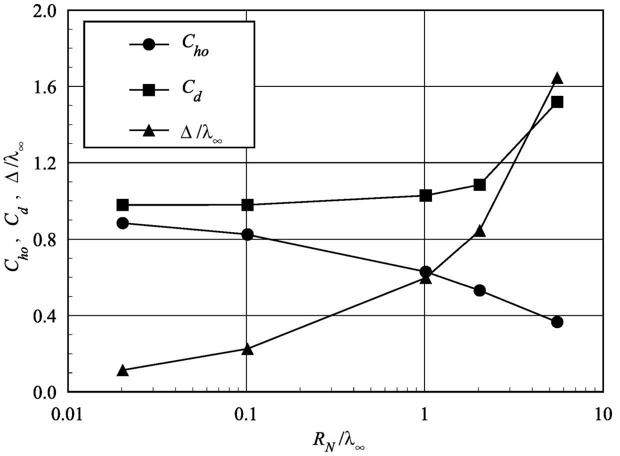

Fig. 18 Heat transfer coefficient at stagnation point C_{h0}, total drag C_d, and shock standoff distance Δ/λ_∞ for round leading edges as a function of nose radius.

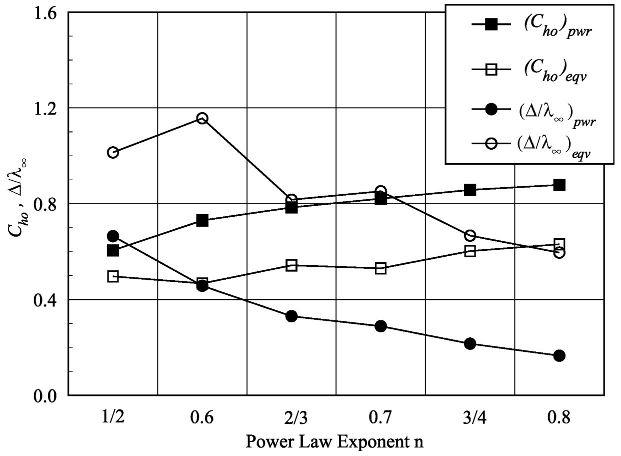

Fig. 20 Comparison of stagnation point heating and shock standoff distance for power law shapes and for equivalent round leading edges that match power law body total drag.

heating is shown in Table 6 and Fig. 19. For comparison, the volume associated with the shapes is also shown in Table 6. Volume is another important geometric comparison related to the active cooling system that may be placed within the leading edge for the purpose of heat absorption. With reference to Table 6, it is seen that equivalent round leading edges have lower drag and smaller shock standoff distance than power law bodies. In addition, equivalent round leading edges provide larger volume than power law shapes. As a reference, the $n = \frac{1}{2}$ case, which is tangent to a 10-deg wedge (Fig. 1), has the same stagnation point heating as a round leading edge that is 4.37 times smaller than the reference round leading edge that is also tangent to the wedge at the same point. Furthermore, this equivalent round leading edge has a volume that is 31.4% larger than the corresponding power law body, the $n = \frac{1}{2}$ case. Consequently, based on Table 6 and Fig. 19, for the same stagnation point heating, round leading edges perform better than power law bodies.

With use of the total drag coefficient C_d found earlier for power law leading edges, an equivalent nose radius $R_{N,\mathrm{eqv}}$ may be found from Fig. 18 that gives the same total drag coefficient as the power law bodies. At this time, the stagnation point heating and the shock standoff distance will be the two important factors to determine which shape is better suited for leading-edge blunting.

The comparison of the stagnation point heating and the shock standoff distance for power law shapes and for round leading edges with equivalent nose radii that match power law body total drag is tabulated in Table 7 and shown in Fig. 20. It is clear from Table 7 that equivalent round leading edges have lower stagnation point heating than the power law bodies. Nevertheless, the equivalent round leading edges have larger shock standoff distance than power law shapes. Again, with the $n = \frac{1}{2}$ case as a reference, this shape has the same total drag as a round leading edge that is around two times smaller than the reference round leading edge. Also, this equivalent round leading edge has a volume that is 10% larger than the corresponding power law body. In contrast, the equivalent round leading edge has

Table 8 Nose radius necessary for comparable shock standoff distance to power law shapes

n	$R_{N,\text{eqv}}/\lambda_\infty$	$R/R_{N,\text{eqv}}$	$C_{h0,\text{eqv}}/C_{h0,\text{pwr}}$	$C_{d,\text{eqv}}/C_{d,\text{pwr}}$	$\bar{V}_{\text{eqv}}/\bar{V}_{\text{pwr}}$
1/2	1.290	4.29	0.997	0.887	1.312
0.6	0.671	8.26	0.963	0.805	1.216
2/3	0.359	15.43	0.981	0.921	1.155
0.7	0.256	21.59	0.963	0.907	1.126
3/4	0.094	58.79	0.967	0.938	1.086
0.8	0.058	95.84	0.974	0.952	1.050

Table 9 Comparison of one-half power law body to round leading edge with the same curvature radius

Parameter	Value
$R_{c,1/2}/\lambda_\infty$	0.962
$R/R_{c,1/2}$	5.759
$C_{h0,\text{eqv}}/C_{h0,1/2}$	1.059
$C_{d,\text{eqv}}/C_{d1/2}$	0.871
$\Delta_{\text{eqv}}/\Delta_{1/2}$	0.866
$\bar{V}_{\text{eqv}}/\bar{V}_{1/2}$	1.338

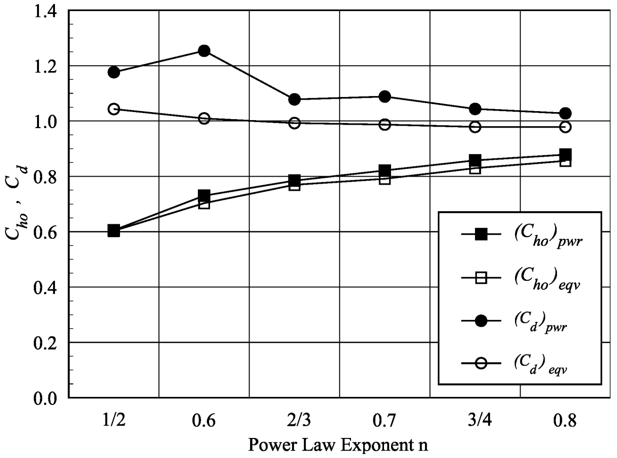

Fig. 21 Comparison of stagnation point heating and total drag coefficient for power law shapes and for equivalent round leading edges that match power law body shock standoff distance.

a shock standoff distance that is around 1.5 times larger than that for the $n = \frac{1}{2}$ case and increases to around 3.6 times for the $n = 0.8$ case, an undesirable property for waveriders as already mentioned. As a result, based on Table 7 and Fig. 20, round leading edges perform worse than power law bodies as the shock standoff distance is taken into consideration.

Another interesting result may be found from the shock standoff distance. The equivalent nose radius $R_{N,\text{eqv}}$ that yields the same shock standoff distance Δ/λ_∞ for each one of the power law shapes may be determined from Fig. 18.

The comparison of the heat transfer coefficient and the total drag coefficient for power law shapes and for round leading edges with equivalent nose radii that match power law body shock standoff distance is tabulated in Table 8 and shown in Fig. 21. It is apparent from Table 8 that equivalent round leading edges provide slightly smaller stagnation point heating and lower total drag than the power law bodies. Furthermore, equivalent round leading edges give larger volume than the power law bodies.

It is important to mention that one-half power law geometry is the only power law geometry with a finite radius of curvature at the leading edge. It is given by $R_c = A^2/2$, where A is defined in Eq. (1). Therefore, the radius of curvature for the $n = \frac{1}{2}$ case is $R_c/\lambda_\infty = 0.962$. A comparison may now be made between the $n = \frac{1}{2}$ case and the round leading edge with the same nose radius. Table 9 presents this comparison for stagnation point heating, total drag, shock standoff distance, and volume. According to Table 9, the round leading edge with the same one-half power law curvature radius provides a smaller total drag, shock standoff distance, and volume than the one-half power law body. Nevertheless, a one-half power law body gives a smaller stagnation point heating than the round leading edge. Figure 1 shows this geometric comparison for the reference round leading edge (circular cylinder) with $R_N/\lambda_\infty = 5.5$, the one-half power law body, and the round leading edge with the same one-half power law nose radius, $R_N/\lambda_\infty = 0.962$. It is apparent that the round leading edge is sharper than the one-half power law body. It is closer to representing the sharp wedge leading edge than the one-half power law body. Usually, as the leading edge shape approaches the sharp wedge leading edge, the total drag decreases, the standoff distance decreases, and the stagnation point heating increases.

Conclusions

The computations of a rarefied hypersonic flow on power law leading edges have been performed by using the DSMC method. The calculations provided information concerning the nature of the stagnation point heating, total drag, and shock wave standoff distance resulting from variations in the body shape. The emphasis of the investigation was to compare power law leading edges with round leading edges to determine which geometry is better suited as a blunting profile. The comparison was based on geometry, stagnation point heating, total drag, and shock wave standoff distance.

Equivalent round leading edges were defined with the same stagnation point heating, total drag, or shock wave standoff distance yielded by power law leading edges. With the same stagnation point heating as power law shapes, round leading edges were shown to produce smaller total drag and smaller shock standoff distance. In addition, results showed that for the same shock standoff distance, round leading edges gave smaller stagnation point heating and smaller total drag. Nevertheless, for the same total drag, power law bodies give smaller shock standoff distance than round leading edges. It is apparent that each comparison resulted in a different conclusion for which geometry performs better. Thus, the ideal blunting leading edge relies on the context. Hence, if shock standoff distance is considered the primary issue in leading-edge design of hypersonic waveriders, then power law leading edges are superior to round leading edges.

References

[1] Nonweiler, T. R. F., "Aerodynamic Problems of Manned Space Vehicles," *Journal of the Royal Aeronautical Society*, Vol. 63, Sept. 1959, pp. 521–528.

[2] Gillum, M. J., and Lewis, M. J., "Experimental Results on a Mach 14 Waverider with Blunt Leading Edges," *Journal of Aircraft*, Vol. 34, No. 3, 1997, pp. 296–303.

[3] Mason, W. H., and Lee, J., "Aerodynamically Blunt and Sharp Bodies," *Journal of Spacecraft and Rockets*, Vol. 31, No. 3, 1994, pp. 378–382.

[4] Santos, W. F. N., and Lewis, M. J., "Power Law Shaped Leading Edges in Rarefied Hypersonic Flow," *Journal of Spacecraft and Rockets*, Vol. 39, No. 6, 2002, pp. 917–925.

[5] Santos, W. F. N., and Lewis, M. J., "Angle of Attack Effect on Rarefied Hypersonic Flow over Power Law Shaped Leading Edges," *Rarefied Gas Dynamics: Proceedings of the 23rd International Symposium on Rarefied Gas Dynamics*, edited by A. D. Ketsdever and E. P. Muntz, AIP Conf. Proceedings, Vol. 663, New York, 2003.

[6] O'Brien, T. F., and Lewis, M. J., "Power Law Shapes for Leading-Edge Blunting with Minimal Shock Standoff," *Journal of Spacecraft and Rockets*, Vol. 36, No. 5, 1999, pp. 653–658.

[7] Santos, W. F. N., "Direct Simulation Monte Carlo of Rarefied Hypersonic Flow on Power Law Shaped Leading Edges," Ph.D. Dissertation, Dept. of Aerospace Engineering, Univ. of Maryland, College Park, MD, Dec. 2001.

[8] Santos, W. F. N., and Lewis, M. J., "Shock Wave Structure in a Rarefied Hypersonic Flow on Power Law Shaped Leading Edges," AIAA Paper 2003-1134, Jan. 2003.

[9] Santos, W. F. N., and Lewis, M. J., "Aerodynamic Heating Performance of Power Law Leading Edges in Rarefied Hypersonic Flow," AIAA Paper 2003-3894, June 2003.

[10] Santos, W. F. N., and Lewis, M. J., "Effects of Compressibility on Rarefied Hypersonic Flow over Power Law Leading Edges," AIAA Paper 2004-1181, Jan. 2004.

[11] Starkey, R. P., and Lewis, M. J., "Simple Analytical Model for Parametric Studies of Hypersonic Waveriders," *Journal of Spacecraft and Rockets*, Vol. 36, No. 4, 1999, pp. 516–523.

[12] Starkey, R. P., and Lewis, M. J., "Analytical Off-Design Lift-to-Drag Ratio Analysis for Hypersonic Waveriders," *Journal of Spacecraft and Rockets*, Vol. 37, No. 5, 2000, pp. 684–691.

[13] Boyd, I. D., and Padilla, J. F., "Simulation of Sharp Leading Edge Aerothermodynamics," AIAA Paper 2003-7062, Dec. 2003.

[14] Anderson, J. L., "Tethered Aerothermodynamic Research for Hypersonic Waveriders," *Proceedings of the 1st International Hypersonic Waverider Symposium*, Univ. of Maryland, College Park, MD, 1990.

[15] Potter, J. L., and Rockaway, J. K., "Aerodynamic Optimization for Hypersonic Flight at Very High Altitudes," *Rarefied Gas Dynamics: Space Science and Engineering*, edited by B. D. Shizgal and D. P. Weaver, Vol. 160, Progress in Astronautics and Aeronautics, AIAA, Washington, DC, 1994, pp. 296–307.

[16] Rault, D. F. G., "Aerodynamic Characteristics of a Hypersonic Viscous Optimized Waverider at High Altitude," *Journal of Spacecraft and Rockets*, Vol. 31, No. 5, 1994, pp. 719–727.

[17] Graves, R. E., and Argrow, B. M., "Aerodynamic Performance of an Osculating-Cones Waverider at High Altitudes," AIAA Paper 2001-2960, 2001.

[18] Bird, G. A., *Molecular Gas Dynamics and the Direct Simulation of Gas Flows*, Oxford Univ. Press, Oxford, 1994.

[19] Bird, G. A., "Monte Carlo Simulation in an Engineering Context," *Rarefied Gas Dynamics*, edited by S. S. Fisher, Pt. 1, Vol. 74, Progress in Astronautics and Aeronautics, AIAA, New York, 1981, pp. 239–255.

[20] Borgnakke, C., and Larsen, P. S., "Statistical Collision Model for Monte Carlo Simulation of Polyatomic Gas Mixture," *Journal of Computational Physics*, Vol. 18, No. 4, 1975, pp. 405–420.

I. Boyd
Associate Editor